MATERIALS SCIENCE

Printable assemblies of perovskite nanocubes on meter-scale panel

Xiao Li[1]*, Zhenjie Xue[1], Xiangyu Chen[2], Xuezhi Qiao[2], Guang Mo[3], Wensheng Bu[2], Bo Guan[2], Tie Wang[1]*

Hierarchical assemblies of functional nanoparticles can have applications exceeding those of individual constituents. Arranging components in a certain order, even at the atomic scale, can result in emergent effects. We demonstrate that printed atomic ordering is achieved in multiscale hierarchical structures, including nanoparticles, superlattices, and macroarrays. The $CsPbBr_3$ perovskite nanocubes self-assemble into superlattices in ordered arrays controlled across 10 scales. These structures behave as single nanoparticles, with diffraction patterns similar to those of single crystals. The assemblies repeat as two-dimensional planar unit cells, forming crystalline superlattice arrays. The fluorescence intensity of these arrays is 5.2 times higher than those of random aggregate arrays. The multiscale coherent states can be printed on a meter-scale panel as a micropixel light-producing layer of primary-color photon emitters. These hierarchical assemblies can boost the performance of optoelectronic devices and enable the development of high-efficiency, directional quantum light sources.

INTRODUCTION

The programmatic design of nanoparticles (NPs) self-assembled into periodic superlattices on large-area substrates offers potential applications in optical, electronic, and catalytic nanodevices (*1*–*4*). Nanofabrication using lithography, chemical etching, and meticulous engineering results in arbitrary geometrical designs and outstanding nanometer-level precision and accuracy (*5*–*8*). Future trends require the progressive development of patterning processes toward larger integration densities and smaller sizes. The NP arrangements formed by bottom-up self-assembly in a nonequilibrium or equilibrium manner are being explored as viable alternatives to standard lithographically patterned devices (*9*). The bottom-up approach is primarily aimed at exploiting the emergent properties of NP assemblies that are notably different from those of the individual constituents or bulk materials (*10*–*13*). These emergent properties have been experimentally confirmed after rationally controlling the interaction of interparticles, composition, stoichiometry, geometry, and crystal structure (*14*–*24*). In these assembled structures, quantum effects can fundamentally change the properties of devices. An ideal method for optimizing the performance of functional nanodevices would involve manipulating the structural organization on multiple scales, from the nano-/microbasic material unit scale down to the atomic scale. To achieve this, precise architectures must be reconciled with accurate spatial placement over large areas. However, such multiscale fabrication precision is beyond the practical and theoretical limits of typical nanotechnology processing. Printing of NPs, an additive manufacturing method, usually cannot modulate the ordering of the atoms in the arrays. Therefore, it is highly desirable to develop alternative fabrication methods and gain previously unidentified insights into the behavior of NP assemblies.

In this study, we first identified and investigated a superperfect NP superlattice with a simple tetragonal structure and lattice alignment that contains densely packed identical perovskite nanocubes with an interparticle distance along the *z* axis that is shorter than those along the *x* and *y* axes. The atomic lattices in each building block are identical over the entire NP superlattice; in other words, every superlattice domain can be treated as a giant single-crystal microcube. A strong coupling effect along the *z* axis induces anisotropic optical properties, causing the NP superlattice to exhibit a uniaxial crystal light body with an oriented transition dipole. NP superlattices can be arranged and spliced by selectively creating prepatterned holes on suitable wafer target sites by an optimized, droplet splitting method using a dispensing machine. This causes each superlattice to orient its *z* axis perpendicularly to the substrate. The long-range order at multiple scales is exhibited as crystalline superlattices that are accurately placed on dozens of areas on the order of square meters, wherein the nanocubes are well organized in the superlattice, and their atoms align in the unified lattices with neighboring nanocubes in atomic order (Fig. 1A). This pattern construction strategy combines the complementary advantages of atomic manipulation and spatial accuracy of bottom-up NP self-assembly with those of top-down nanofabrication. This strategy can be extended using three monochromatic NP superlattices to precisely define topographic characteristics that are distributed arbitrarily onto a large surface.

RESULTS

Suitable $CsPbBr_3$ nanocubes were synthesized using a previously described method (*25*, *26*), with modifications that included thermal decomposition of $PbBr_2$ and cesium oleate in the presence of oleylamine and oleic acid at 170°C. The synthesis yielded monodisperse nanocubes with the average length of 7.2 ± 0.3 nm and peak absorption and emission at 495 and 506 nm, respectively (fig. S1), as statistically determined using transmission electron microscopy (TEM) (Fig. 1B and fig. S2; see Materials and Methods for details). The orthorhombic phase of $CsPbBr_3$ nanocubes was verified using x-ray powder diffraction (XRD) (space group *Pbnm*, $a = 8.218$ Å, $b = 8.256$ Å, and $c = 11.734$ Å; fig. S3 and table S1). These perovskite crystals consisted of corner-sharing PbX_6 octahedra and Cs^+ ions filling the voids (*16*), inducing a strong linear dipole polarized along the *z* axis to

[1]Life and Health Intelligent Research Institute, School of Chemistry and Chemical Engineering, Tianjin University of Technology, Tianjin 300384, P. R. China. [2]Beijing National Laboratory for Molecular Sciences, Institute of Chemistry, Chinese Academy of Sciences, Beijing 100190, P. R. China. [3]Beijing Synchrotron Radiation Facility, Institute of High Energy Physics, Chinese Academy of Sciences, Beijing 100049, P. R. China. *Corresponding author. Email: lixiao@email.tjut.edu.cn; wangtie@email.tjut.edu.cn

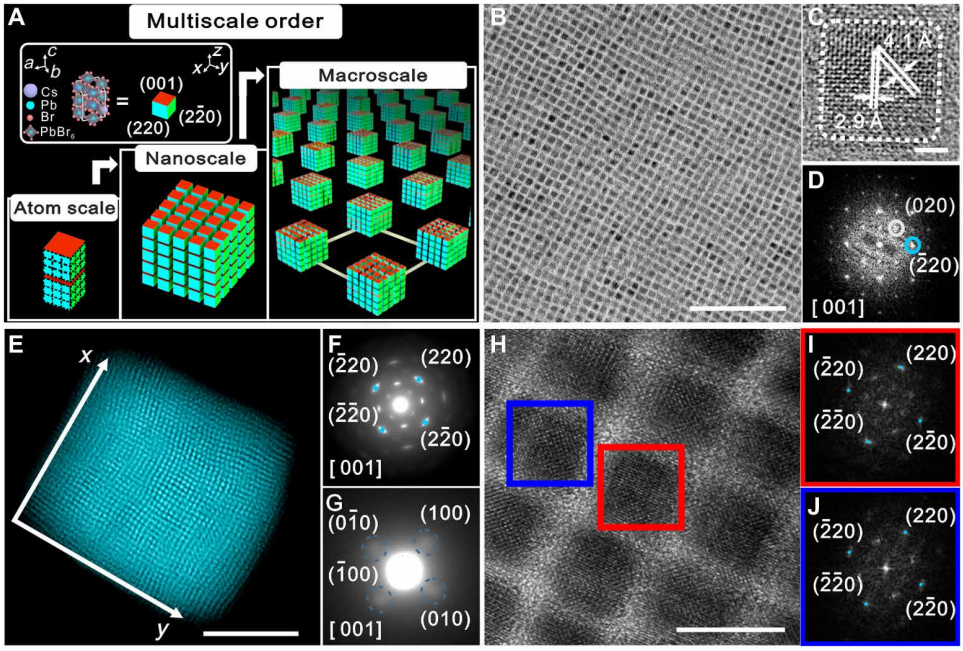

Fig. 1. Structural analysis of nanocubes and their superlattices. (**A**) Schematic of a mazing long-range order across the multiscale: crystalline superlattices accurately placed on dozens of substrate areas in the order of square centimeters, NPs are well organized in a superlattice, and their atoms align a unified lattice with neighboring NPs to have the atomic order. (**B**) Typical transmission electron microscopy (TEM) image of the $CsPbBr_3$ NPs with an average edge length of approximately 7.2 nm. Scale bar, 100 nm. (**C**) High-resolution TEM (HR-TEM) images of $CsPbBr_3$ NPs projected along the $[001]_{NP}$ direction showing the atomic fringes with d-spacings of 2.9 and 4.1 Å. Scale bar, 2 nm. (**D**) Corresponding fast Fourier transform (FFT) pattern of (C). (**E**) Representative high-angle annular dark-field scanning TEM of individual superlattices projected along the *z* direction. Scale bar, 200 nm. (**F**) Typical corresponding wide-angle electron diffraction image with main $(220)_{NP}$ facets. (**G**) Typical corresponding SAED image. (**H**) HR-TEM images of adjacent local NPs in superlattices. Scale bar, 10 nm. (**I** and **J**) The corresponding FFT patterns of superlattice located at the positions of the red and blue squares in (H).

align the nanocubes. The well-resolved interfringe distances of 0.29 and 0.41 nm were also indexed to the (220) and (020) lattice planes, respectively, of orthorhombic $CsPbBr_3$ (Fig. 1, C and D, and fig. S4). Fast Fourier transform (FFT) analyses suggested that the square basal plane in each $CsPbBr_3$ nanocube was normal with respect to the <001> direction, wherein the four faces were formed by (220) planes (Fig. 1D and fig. S4).

The NP superlattices were induced by slow evaporation of the solvent in an airtight storage tank filled with *n*-hexane vapor (see Materials and Methods for details). This procedure led to the aggregation of nanocubes and the gradual formation of individual superlattices with a square geometry, as well as the eventual precipitation on TEM grids or silicon wafers pretreated by reactive ion etching using HBr. Superlattices, with different lateral sizes ranging from 0.5 to 10 μm, were prepared by tuning the evaporation speed of the solvent and the concentration of the nanocubes (Fig. 1E and fig. S5). The periodicity of the superlattices is relative to the small-angle selected-area electron diffraction (SAED) region, whereas atomic periodicity is reflected in the wide-angle electron diffraction region (*27*, *28*). The spot-type texture (as opposed to a full-ring texture) in both electron diffraction regions demonstrates that the atomic lattice alignment extends to the entire superlattice (Fig. 1, F and G). High-resolution TEM (HR-TEM) observations and FFT analyses further showed that the superlattices were highly ordered on the atomic scale (Fig. 1, H to J, and fig. S6). All the nanocubes were directed along the <001> axis perpendicular to the *xy* plane of the square superlattice and laterally connected via the in-plane {220} facets of the nanocubes (figs. S7 and S8). The interparticle distance of 10.2 nm was identical along both the *x* and *y* axes; however, this distance was larger than the value of 9.0 nm along the *z* axis (Figs. 1E and 2A and fig. S5). This variation in distance can be attributed to the larger number of terminations in the (001) facets, as verified by the electron energy loss spectroscopy chemical maps (figs. S9 and S10). These bromine-rich surfaces resulted in the weak attachment of oleate ligands (fig. S11). Partial ligands were detached from the (001) facets and absorbed in the solvent, leading to a reduced interparticle distance. The grazing-incidence small-angle x-ray scattering (GISAXS) measurement of the NP superlattices indicated a simple tetragonal (001) vertical crystallographic orientation with respect to the silicon substrate, as shown in Fig. 2A.

To obtain detailed understanding of the formation process for NP superlattice, both real time and in situ, we performed GISAXS to obtain structural information (Fig. 2A). Structure formation progresses in four stages: amorphous phase (I), simple cubic phase (II), transitional phase (III), and simple tetragonal phase (IV) (Fig. 2, B to D, and fig. S12). In stage I, there were no rings or dots displayed for the long-range NP orientation or atomic arrangement. After 1.5 min, when the assembly process moved to stage II, diffraction rings appeared at an equal distance in q_x, q_y, and q_z, which was indexed as simple cubic superlattices with lattice parameters of $a = b = c = 10.8 \pm 0.1$ nm (see fig. S13 and table S2 for indexation). After a long interval, there was a transition from the simple cubic structure to the final simple tetragonal phase at stage III. The diffraction rings began to transform into arcs, indicating a better crystallographic orientation. A new bright spot gradually appeared at a larger q_z value, owing to the decrease in the interparticle distance

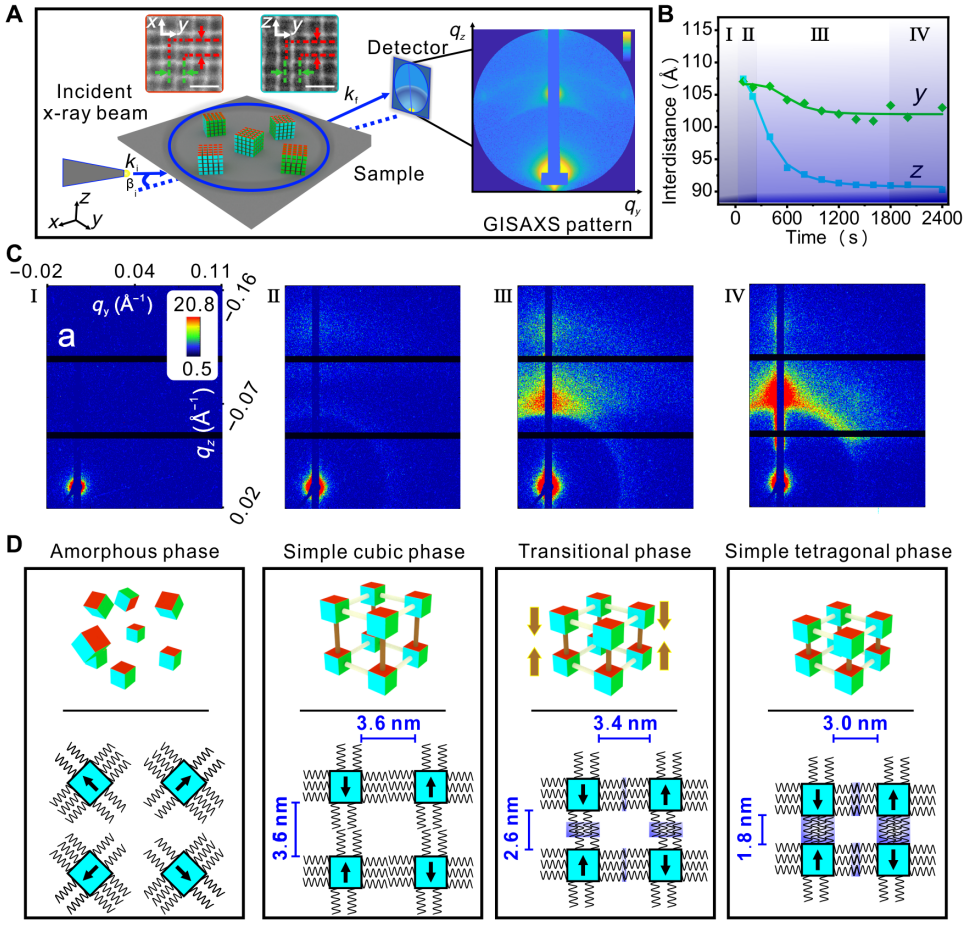

Fig. 2. Different stages of progress toward a simple tetragonal superlattice. (**A**) Schematic of the sample placed in the grazing-incidence small-angle scattering (GISAXS). The incident beam of wave vector k_i makes a small incident angle β_i with respect to the sample surface. GISAXS probes the scattered intensity close to the specularly reflected beam. The top left inset is a typical TEM image of NPs projected along the *z* direction showing equal interdistances along the *x* and *y* axes. The top right inset is a typical TEM image of NPs projected along the *x* direction showing shorter interdistance along the *z* axis of the superlattices than along the *y* axis. The right inset contains the typical GISAXS pattern: arc with a high *q* spot in the *z* direction and obliquely superior spots on both sides. Scale bars, 20 nm. (**B**) Interdistance between NPs along *y* and *z* axes directions as a function of time. (**C**) Temporal evolution of GISAXS patterns during the in situ measurement of the self-assembly of the NPs, showing the transition from a colloidal suspension to an equal spacing superlattice to a compressed superlattice via contraction of the *c* axis. (**D**) Overall depiction of the consecutive phase transitions during the self-assembly of NPs. The black arrows represent the dipole moment direction of single NPs along the *c* axis. The blue rectangle regions represent the range of the interligand interdigitation.

along the *z* direction. At stage IV, the NP superlattices reached their final simple tetragonal structure, where a significant contraction occurred along the *c* axis, whereas the distances between the nanocrystals along the *a* and *b* axes remained equal (fig. S14). The drastic decrease in length along the *c* axis can be attributed to ligand interdigitation owing to the detachment of partial ligands in the (001) facets of the nanocubes (Fig. 2D). The simple tetragonal superlattices had unit cell constants $a = b = 10.2 \pm 0.1$ nm and $c = 9.0 \pm 0.1$ nm (see fig. S15 and table S3 for indexation). The grazing-incidence wide-angle x-ray (GIWAXS) patterns of the NP superlattices demonstrated sharp, sporadic Bragg spots, whereas the out-of-plane mode of the XRD patterns showed clear periodic crystallographic planes, indicating the vertical crystallographic orientation of the *z* axis with respect to the substrate (fig. S16, A to D). Pre-adlayers of bromine anions on the surface increased the dipole-dipole attraction between the $CsPbBr_3$ nanocrystals and substrates, which may have played a key role in guiding the preferential NPs orientation. In contrast, the crystallographic planes disappeared when NP superlattices were formed on the substrate without pre-adlayers of bromine anions. Furthermore, the GIWAXS patterns switched to diffraction rings, accompanied by randomly oriented crystals (fig. S16, E to H).

The adjusted *z* axis of the superlattice features inspired us to print large-area crystalline superlattice arrays by a droplet splitting method using a dispensing machine and by a lithography etching technique (Fig. 3A). We first designed a variety of micrometer-level grooves on the substrate by photolithography etching, after which the liquid in the needle of the dispensing machine was injected into the appropriate groove sites by controlling the dispensing pressure level during the up and down movement of the needle along the *z* axis (Fig. 3B). During the injection process, solvent evaporation control caused the NPs to nucleate in the cube grooves and eventually aggregated (*17*, *29*). The concave structure provided a confined environment that drastically decreased the nucleation barrier for the assembly of nanocubes in topographical traps (Fig. 3B) (*15*). The

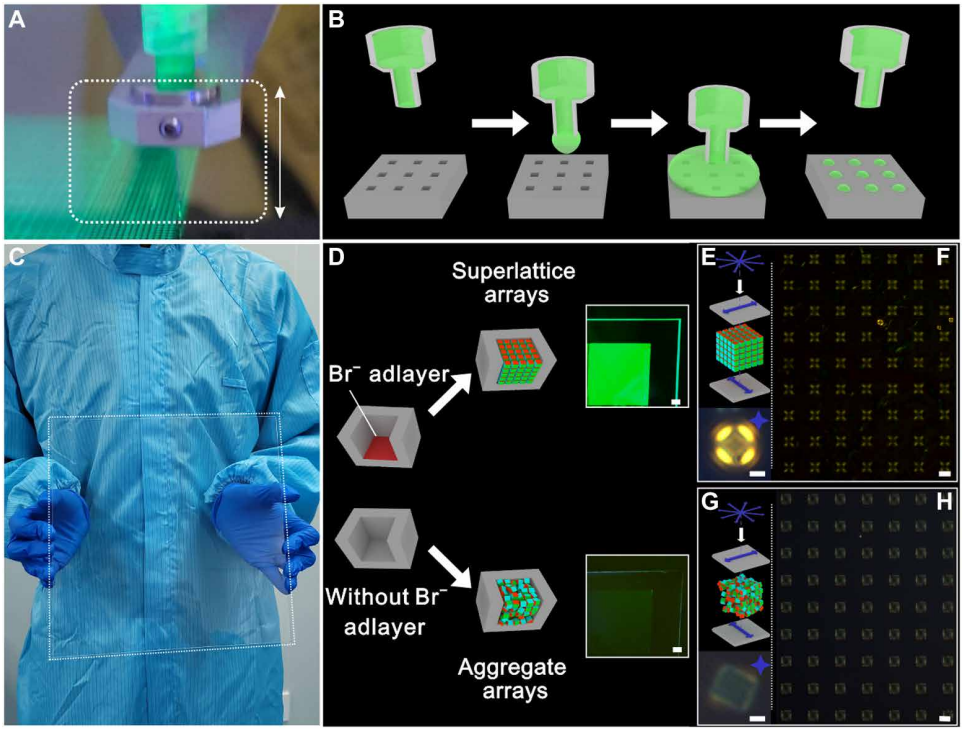

Fig. 3. Packing of superlattices into crystalline superlattice arrays with *z* axis pointing upward. (**A**) Photograph of optimized dispensing machine for specific site arrays in operation. (**B**) The combination of the dispensing process and the grooved substrate to obtain the array. The NP solution was injected into the groove at the specific site of the substrate through the up and down movement of the high-precision needle along the *z* direction. (**C**) Photograph of the assembled meter-level crystalline superlattice array. Because of the low content, the luminous layer cannot be seen by the naked eye under the sunlight. (**D**) Schematic of the formation of crystalline superlattice array and aggregate array when patterned cube grooves are functionalized with or without adlayers of bromine anions, respectively. The insets are the corresponding fluorescence micrographs. The high brightness of the crystalline superlattice array panel can be recognized. Scale bars, 1 cm. Schematic of the flat superlattices along a *z* axis perpendicular to the sample stage plane (**E**) and random nanocube aggregates arrays (**G**) placed into crossed polarizers with the conoscope lens (top) and the corresponding polarized optical microscopes (bottom). Scale bars, 2 μm. Polarized optical microscopy of crystalline superlattices array chips (**F**) and random nanocube aggregates array chips (**H**). Scale bars, 10 μm.

precision spitting tip of the needle was moved in the *xy* plane with tens of thousands of repetitive injections to splice the micrometer arrays and then the meter-scale panel. When the cubic grooves in the substrate were densely functionalized by bromine anions, the nanocubes tended to form crystalline superlattice arrays (Fig. 3, C and D). The size and shape of the grooves and the pressure of the injection of the dispensing machine were not the main factors influencing the atomic ordering of the superlattice arrays (fig. S17). The presence of crystalline superlattice arrays was further confirmed using a polarizing microscope with a conoscope lens. For the NP superlattices, a Maltese cross birefringence with an interference color circle was observed (Fig. 3E) when the *z* axis was perpendicular to the substrate. In contrast, no Maltese cross birefringence was observed when the orientation of the *z* axis was changed (Fig. 3G). Anisotropic NP-superlattice arrays with Maltese cross birefringence extending over the micrometer scale were visible on the surface of the pattern zone (Fig. 3F). Each cube groove contained, on average, tens of thousands of uniformly aligned nanocubes, with the NP-superlattice arrays spanning the entire range of the wafer, and the *z* axis orientations aligned vertically toward the substrate (fig. S18).

The hierarchical assemblies were composed of crystalline arrays of anisotropic ordered superlattices packed with NPs that had consistent atomic orientations. These assemblies can be used as the basis of a promising strategy for enhancing the performance of microlight-emitting devices (*30*, *31*). We found that this structure increases the brightness of backlight panels of NPs. The NPs normally exhibit excellent brightness characteristics at the single-particle level; however, the brightness decreases if the NPs are aggregated in a disorderly fashion into films. Currently, the pixels of backlight panels are typically composed of randomly aggregated NPs (*30*). Random NP aggregates typically emit photons in all directions and exhibit low brightness owing to insufficient convergence (Fig. 4A). However, when the NPs in this study were assembled into anisotropic simple tetragonal superlattices, the resulting crystalline superlattice arrays were approximately 5.2 times brighter than arrays of random NP aggregates, after normalizing the quality (Fig. 4B and figs. S19 to S21). This brightness enhancement can be attributed to a combination of the directional dielectric-antenna effect inside the uniaxially coupled superlattice patterns and photon redistribution induced by oriented transition dipoles in macro panels (*32*–*34*). To verify this conjecture, we performed a linearly polarized photoluminescence (PL) emission test at 517 nm. A typical emission polarization ratio calculated using $P_{emi} = (I_{max} - I_{min})/(I_{max} + I_{min})$ was approximately 0.66 (Fig. 4C); this value is comparable to that of individual CdSe-CdS nanorods (0.75) (*35*, *36*). This suggests that the transition dipole in the arrays was highly oriented (fig. S22).

Various programmable metamaterials with ultrahigh-brightness crystalline superlattice arrays were fabricated using lithography to

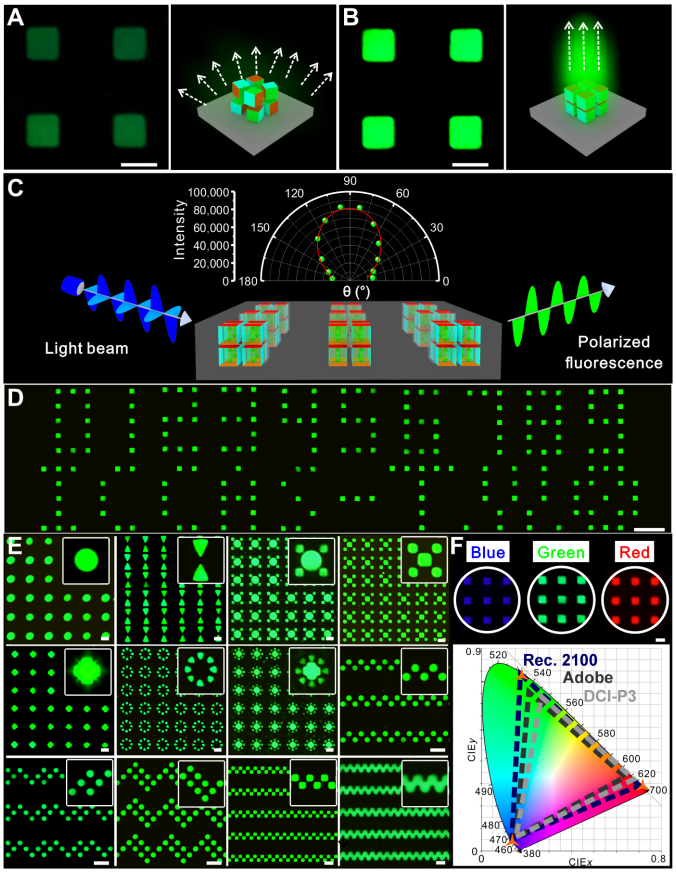

Fig. 4. Microbacklit display of crystalline superlattice arrays. (**A**) PL microscopy images of random nanocube aggregates in pixels. Scale bar, 10 μm. (**B**) PL microscopic images of the simple tetragonal phase nanocube superlattices in pixels. Scale bar, 10 μm. (**C**) Schematic of the identical strong coupling along the *z* axis of crystalline superlattice array–induced polarized light emission along *z* axis. The green arrows are the transition dipole direction. The inset is the azimuthal plot of the PL intensity response versus the emission polarization angle when measuring the crystalline superlattice arrays under an excitation wavelength of 360 nm. (**D**) The collection of fluorescence micrographs includes the Arabic numeral characters (0 to 9) (top) and the capital letters (ICCAS TW) (bottom) of crystalline superlattice arrays. Scale bar, 100 μm. (**E**) Various topographical structure shapes of crystalline superlattice arrays. Scale bars, 10 μm. The insets are the enlarged images. (**F**) Commission Internationale de l'Eclairage (CIE) 1931 coordinates of the three monochromatic primaries of crystalline superlattice arrays compared to the current color standards. The insets are the fluorescence micrographs of three monochromatic primaries. Scale bar, 10 μm.

adjust the topographical structure of silicon wafers. These materials exhibited large-scale topology regulation (Fig. 4, D and E, and fig. S23). We also assembled red and blue arrays of the crystalline superlattice with enhanced PL by tuning the precursor mixture ratios of Br^-/I^- and Br^-/Cl^- for other halogen-type nanocubes. Three monochromatic primary PL colors were successfully achieved using the Commission Internationale de l'Eclairage (CIE) 1931 color coordinates of (0.137, 0.047) for ultrapure blue, (0.174, 0.779) for ultrapure green, and (0.712, 0.287) for ultrapure red, which represents 97.2% color saturation per the Rec. 2100 standard (100.4% per the CIE 1976 color space), thereby demonstrating the ultrawide color display (Fig. 4F, fig. S24, and table S4). These results can be attributed to the superperfect superlattice arrays with lattice consistency produced by hierarchical transformation of the NPs, superlattices, and macroarrays (fig. S25).

DISCUSSION

From a fundamental perspective, superperfect assemblies with uniaxial orientation displayed previously unachieved accurate spatial placement across the centimeter, nanometer, and atomic scales, resulting in strong emission bursts. Transformations from simple cubic to simple tetragonal crystalline structures have been achieved. An understanding of the successive stages of assembly dynamics was gained through in situ monitoring. Crystalline superlattice arrays have proven emergent effects along the *c* axis, resulting in optical properties that exceed those of the individual building blocks and random aggregates. Parallels in the behavior of green, red, and blue perovskite nanocubes suggest a possible fundamental universality. The large-area ordering of NP assemblies can be regulated by the substrate components, which is conducive to the development of long-range ordering of other semiconductors and metal or dielectric NP assemblies. Theoretically, template-assisted printing assemblies can be used to engineer sophisticated superperfect assembled systems, which will help meet the demand for high-brightness and multiphoton quantum light sources, as well as potentially exploit the next-generation miniaturization of light-emitting displays toward arbitrary surface patterns, high polarization, ultrahigh brightness, and an ultrawide color gamut.

MATERIALS AND METHODS

Synthesis and purification of $CsPbBr_3$, $CsPbCl_3$, and $CsPbI_3$ NPs

In the typical synthesis of $CsPbBr_3$, 15.0 ml of octadecene (ODE), 207.0 mg of $PbBr_2$, 1.5 ml of oleylamine, and 1.5 ml of oleic acid in a three-neck flask were mixed under vacuum and heated up to 120°C for 1 hour (*25*, *26*). The above mixture was subsequently heated to 170°C under argon and kept for 20 min, which was followed by a swift injection of 1.2 ml of the cesium oleate solution. The crude solution was cooled immediately to room temperature with the cold air gun and subsequently centrifuged at 7000 rpm for 4 min. After centrifugation, the precipitation was discarded. The supernatant solution was mixed with 60 ml of toluene, forming stable colloidal solutions, and stored at 22°C for 3 days. The resulting solution was purified by antisolvent ethyl acetate with a ratio of 1:3 to achieve precipitation of the NPs. The purified NPs were stored for the next preparation of superlattices.

As for $CsPbCl_3$ NPs, 20.0 ml of ODE, 241.3 mg of $PbCl_2$, 1.0 ml of oleic acid, 20.4 mg of 2,2'-Iminodibenzoic acid (IDA), and 2.0 ml of oleylamine in a three-neck flask were mixed and heated up to 120°C under vacuum for 45 min. The above mixture was subsequently heated to 170°C under argon and kept for 20 min, which is followed by a swift injection of 1.2 ml of the cesium oleate solution. The other steps are the same as $CsPbBr_3$.

As for $CsPbI_3$ NPs, 15.0 ml of ODE, 402 mg of PbI_2, 3.5 ml of oleylamine, 20 mg of IDA, and 1.5 ml of oleic acid in a three-neck flask were mixed and heated up to 120°C under vacuum for 45 min. The above mixture was subsequently heated to 170°C under argon and kept for 20 min, which is followed by a swift injection of 1.2 ml of the cesium oleate solution. The other steps are the same as $CsPbBr_3$.

Assembly of NPs

The superlattices were created through solvent (hexane) evaporation in an airtight storage tank. Different lateral size superlattices were prepared by tuning the evaporation speed solvent and the concentration of the nanocrystals.

For the lateral 0.5-μm by 0.5-μm superlattices, an *n*-hexane solution containing NPs with sizes of side length = 7.2 nm (2 mg/ml, 5 μl) was dropped onto the carbon support film. The evaporation was complete within 30 min. For the lateral 1-μm by 1-μm superlattices, 30 μl of solution of NPs in *n*-hexane (6 mg/ml) was dropped onto the 1.5-cm by 1.5-cm silicon wafer under the atmosphere of *n*-hexane vapor and volatilized slowly for 24 hours. For the lateral 5-μm by 5-μm superlattices, 30 μl of solution of NPs in *n*-hexane (6 mg/ml) was dropped onto the 1.5-cm by 1.5-cm silicon wafer under the atmosphere of *n*-hexane vapor and volatilized slowly for 72 hours. For the lateral 10-μm by 10-μm superlattices, 30 μl of solution of NPs in *n*-hexane (6 mg/ml) was dropped onto the 1.5-cm by 1.5-cm silicon wafer under the atmosphere of *n*-hexane vapor and volatilized slowly for 96 hours.

Crystalline superlattice arrays

The topographic structure substrate of P <100> silicon with the mask was treated by the reactive ion etching of HBr. After the process of removing the mask, 30 μl of solution of NPs in *n*-hexane (10 mg/ml) was dropped onto the various topographic structure of a 1.5-cm by 1.5-cm wafer under the atmosphere of *n*-hexane vapor and volatilized slowly for 96 hours.

Random nanocube aggregates arrays

Ten microliters of solution of NPs in *n*-hexane (10 mg/ml) was directly dropped onto the topographic structure of a 1.5-cm by 1.5-cm substrate wafer under the atmosphere of *n*-hexane vapor. The above operation was repeated three times at intervals of 5 min. Then, they were volatilized for 96 hours.

Large-area crystalline superlattice arrays by optimized dispensing and photolithography etching technology

The inner diameter of the needle of the injection cavity of the dispensing machine was preferably 60 μm, and the length of the flow channel was preferably 55 mm. The tip of the needle was further ground before use. The pressure of the dispensing machine is set to 1 kPa. To control the volatilization rate, the dispensing device is covered by a closed acrylic shell. Two *n*-hexane atomizers were placed around the confined space. The solvent is preferably *n*-undecane. The topographic structure substrate with the mask was treated by the reactive ion etching of HBr. After the process of removing the mask, a solution of NPs in *n*-undecane (10 mg/ml) in the injection cavity was injected onto the various topographic structure of the substrate during the up and down movement of the needle along the *z* axis. The precision spit tip moves in the *xy* plane with tens of thousands of repetitive injections to achieve the splicing of micrometer arrays and then meter-level panels. The panels were then volatilized slowly for 96 hours.

Characterization and measurement

The morphology of the obtained products was performed using TEM on JEOL JEM-1011 with a thermionic gun operating at 100 kV of accelerating voltage and HR-TEM images on JEOL JEM-2100F working at an accelerating voltage of 200 kV. SAED patterns were taken with TEM on JEM-1011 with different camera lengths. Samples were prepared by dropping washed and diluted NP solutions onto carbon-coated 200-mesh copper grids with subsequent solvent evaporation in a vacuum.

Scanning electron micrographs together with energy-dispersed x-ray spectroscopy measurements were performed on a Hitachi S-4800 field-emission scanning electron microscope. Electron energy loss spectroscopy was recorded using a Gatan Quantum spectrometer installed on a Themis 300 microscope.

Powder XRD patterns of the obtained products were measured on a PANalytical Empyrean-2 x-ray diffractometer using Cu Kα source with a 1/2° fixed diffraction slit and a 1-mm receiver slit. Ultraviolet-visible absorbance spectra were recorded with a Shimadzu UV-1800 spectrophotometer. The PL measurements were acquired using an RF-5301PC spectrofluorophotometer with emission and excitation slit widths of 1.5 nm and an excitation wavelength of 360 nm. Cross-polarized optical images were collected using Olympus BX51-P. Fluorescence micrographs were collected using Olympus IX 83. PL emission polarization was conducted on the FLS 980 spectrofluorometer. Raman spectra and PL emission spectra of single pixel were conducted on the Horiba LabRAM HR Evolution.

The GISAXS measurements under the experimental conditions of a 0.154-nm incident x-ray wavelength and a distance of 250 cm between the sample chamber and the two-dimensional charge-coupled device (CCD) camera (Mar 165) were carried out in a 1W2A beamline at BSRF (Beijing Synchrotron Radiation Facility). A thin Pb strip was used to be a beam stop. Spot size is 10 mm by 5 mm. The GIWAXS measurements were also performed at the 1W2A beamline of BSRF. Spot size is 10 mm by 5 mm. The transmission mode small-angle x-ray scattering measurements were conducted at the Xeuss 2.0 with a PILATUS3 300K CCD camera. The distance between the sample and the detector was set to 250 cm.

The in situ GISAXS measurements were also conducted using the Xeuss 2.0 with the PILATUS3 300K CCD camera. The sample-to-detector distances were calibrated from the theoretical value of the characteristic peak of the standard silver behenate ($AgC_{22}H_{43}O_2$) crystal, $q_{(001)} = 1.07\ nm^{-1}$. The grazing angle was set as 0.8° for achieving the optimal signal-to-noise ratio. The x-ray exposure time of the sample was set to 60 s. The sample compartment was a custom-made, vacuum-able, sealed aluminum chamber with windows that enabled the x-ray beam to be directed at the sample while allowing the scattered signal to enter the detector through another window. The sample compartment had a viewing window for ease of observation. A weighing bottle containing 2 ml of hexane was placed at the corners of the chamber before the sample was placed, and the entire chamber was sealed and allowed to stand for 20 min to saturate the chamber with hexane vapor. The NP dispersion was then added dropwise to the substrate. To slow down the volatilization of the NP dispersion, a trace amount of ODE was usually added to the NP dispersion, allowing us to obtain the NP packing information until up to 40 min.

SUPPLEMENTARY MATERIALS

Supplementary material for this article is available at https://science.org/doi/10.1126/sciadv.add1559

REFERENCES AND NOTES

1. C. T. Black, C. B. Murray, R. L. Sandstrom, S. Sun, Spin-dependent tunneling in self-assembled cobalt-nanocrystal superlattices. *Science* **290**, 1131–1134 (2000).

2. T. Wang, J. Zhuang, J. Lynch, O. Chen, Z. Wang, X. Wang, D. LaMontagne, H. Wu, Z. Wang, Y. C. Cao, Self-assembled colloidal superparticles from nanorods. *Science* **338**, 358–363 (2012).
3. L. Zhou, Y. Tan, J. Wang, W. Xu, Y. Yuan, W. Cai, S. Zhu, J. Zhu, 3D self-assembly of aluminium nanoparticles for plasmon-enhanced solar desalination. *Nat. Photonics* **10**, 393–398 (2016).
4. Y. Sun, S. Dai, High-entropy materials for catalysis: A new frontier. *Sci. Adv.* **7**, eabg1600 (2021).
5. C. Yi, H. Liu, S. Zhang, Y. Yang, Y. Zhang, Z. Lu, E. Kumacheva, Z. Nie, Self-limiting directional nanoparticle bonding governed by reaction stoichiometry. *Science* **369**, 1369–1374 (2020).
6. Z. Tang, N. A. Kotov, M. Giersig, Spontaneous organization of single CdTe nanoparticles into luminescent nanowires. *Science* **297**, 237–240 (2002).
7. C. H. Huang, X. Y. Chen, Z. J. Xue, T. Wang, Effect of structure: A new insight into nanoparticle assemblies from inanimate to animate. *Sci. Adv.* **6**, eaba1321 (2020).
8. D. Vila-Liarte, M. W. Feil, A. Manzi, J. L. Garcia-Pomar, H. Huang, M. Döblinger, L. M. Liz-Marzán, J. Feldmann, L. Polavarapu, A. Mihi, Templated-assembly of $CsPbBr_3$ perovskite nanocrystals into 2D photonic supercrystals with amplified spontaneous emission. *Angew. Chem. Int. Ed. Engl.* **59**, 17750–17756 (2020).
9. K. J. Si, Y. Chen, Q. Shi, W. Cheng, Nanoparticle superlattices: The roles of soft ligands. *Adv. Sci.* **5**, 1700179 (2018).
10. T. Chen, M. Pauly, P. M. Reis, A reprogrammable mechanical metamaterial with stable memory. *Nature* **589**, 386–390 (2021).
11. Y. Nagaoka, R. Tan, R. Li, H. Zhu, D. Eggert, Y. A. Wu, Y. Liu, Z. Wang, O. Chen, Superstructures generated from truncated tetrahedral quantum dots. *Nature* **561**, 378–382 (2018).
12. V. N. Manoharan, Colloidal matter: Packing, geometry, and entropy. *Science* **349**, 1253751 (2015).
13. X. Li, Z. Lu, T. Wang, Self-assembly of semiconductor nanoparticles toward emergent behaviors on fluorescence. *Nano Res.* **14**, 1233–1243 (2021).
14. A. P. Alivisatos, K. P. Johnsson, X. Peng, T. E. Wilson, C. J. Loweth, M. P. Bruchez, P. G. Schultz, Organization of 'nanocrystal molecules' using DNA. *Nature* **382**, 609–611 (1996).
15. R. Su, S. Ghosh, T. C. H. Liew, Q. Xiong, Optical switching of topological phase in a perovskite polariton lattice. *Sci. Adv.* **7**, eabf8049 (2021).
16. M. A. Becker, R. Vaxenburg, G. Nedelcu, P. C. Sercel, A. Shabaev, M. J. Mehl, J. G. Michopoulos, S. G. Lambrakos, N. Bernstein, J. L. Lyons, T. Stöferle, R. F. Mahrt, M. V. Kovalenko, D. J. Norris, G. Rainò, A. L. Efros, Bright triplet excitons in caesium lead halide perovskites. *Nature* **553**, 189–193 (2018).
17. S. Kumar, T. Marcato, F. Krumeich, Y.-T. Li, Y.-C. Chiu, C.-J. Shih, Anisotropic nanocrystal superlattices overcoming intrinsic light outcoupling efficiency limit in perovskite quantum dot light-emitting diodes. *Nat. Commun.* **13**, 2106 (2022).
18. W. Xu, W. Liu, J. F. Schmidt, W. Zhao, X. Lu, T. Raab, C. Diederichs, W. Gao, D. V. Seletskiy, Q. Xiong, Correlated fluorescence blinking in two-dimensional semiconductor heterostructures. *Nature* **541**, 62–67 (2017).
19. D. Lapkin, C. Kirsch, J. Hiller, D. Andrienko, D. Assalauova, K. Braun, J. Carnis, Y. Y. Kim, M. Mandal, A. Maier, A. J. Meixner, N. Mukharamova, M. Scheele, F. Schreiber, M. Sprung, J. Wahl, S. Westendorf, I. A. Zaluzhnyy, I. A. Vartanyants, Spatially resolved fluorescence of caesium lead halide perovskite supercrystals reveals quasi-atomic behavior of nanocrystals. *Nat. Commun.* **13**, 892 (2022).
20. G. Liu, S. H. Petrosko, Z. Zheng, C. A. Mirkin, Evolution of Dip-Pen nanolithography (DPN): From molecular patterning to materials discovery. *Chem. Rev.* **120**, 6009–6047 (2020).
21. P. J. Santos, P. A. Gabrys, L. Z. Zornberg, M. S. Lee, R. J. Macfarlane, Macroscopic materials assembled from nanoparticle superlattices. *Nature* **591**, 586–591 (2021).
22. A. Dong, J. Chen, S. J. Oh, W.-K. Koh, F. X. Xiu, X. C. Ye, D.-K. Ko, K. L. Wang, C. R. Kagan, C. B. Murray, Multiscale periodic assembly of striped nanocrystal superlattice films on a liquid surface. *Nano Lett.* **11**, 841–846 (2011).
23. Y. Nagaoka, K. Hills-Kimball, R. Tan, R. P. Li, Z. W. Wang, O. Chen, Nanocube superlattices of cesium lead bromide perovskites and pressure-induced phase transformations at atomic and mesoscale levels. *Adv. Mater.* **29**, 1606666 (2017).
24. X. Zheng, W. Smith, J. Jackson, B. Moran, H. Cui, D. Chen, J. Ye, N. Fang, N. Rodriguez, T. Weisgraber, C. M. Spadaccini, Multiscale metallic metamaterials. *Nat. Mater.* **15**, 1100–1106 (2016).
25. L. Protesescu, S. Yakunin, M. I. Bodnarchuk, F. Krieg, R. Caputo, C. H. Hendon, R. X. Yang, A. Walsh, M. V. Kovalenko, Nanocrystals of cesium lead halide perovskites ($CsPbX_3$, X = Cl, Br, and I): Novel optoelectronic materials showing bright emission with wide color gamut. *Nano Lett.* **15**, 3692–3696 (2015).
26. Y. Wang, X. Li, J. Song, L. Xiao, H. Zeng, H. Sun, All-inorganic colloidal perovskite quantum dots: A new class of lasing materials with favorable characteristics. *Adv. Mater.* **27**, 7101–7108 (2015).
27. M. Chen, J. Kim, J. P. Liu, H. Fan, S. Sun, Synthesis of FePt nanocubes and their oriented self-assembly. *J. Am. Chem. Soc.* **128**, 7132–7133 (2006).
28. J. J. Geuchies, C. van Overbeek, W. H. Evers, B. Goris, A. de Backer, A. P. Gantapara, F. T. Rabouw, J. Hilhorst, J. L. Peters, O. Konovalov, A. V. Petukhov, M. Dijkstra, L. D. A. Siebbeles, S. van Aert, S. Bals, D. Vanmaekelbergh, In situ study of the formation mechanism of two-dimensional superlattices from PbSe nanocrystals. *Nat. Mater.* **15**, 1248–1254 (2016).
29. Q.-Y. Lin, J. A. Mason, Z. Y. Li, W. J. Zhou, M. N. O'Brien, K. A. Brown, M. R. Jones, S. Butun, B. Lee, V. P. Dravid, K. Aydin, C. A. Mirkin, Building superlattices from individual nanoparticles via template-confined DNA-mediated assembly. *Science* **359**, 669–672 (2018).
30. Z. Liu, C.-H. Lin, B.-R. Hyun, C.-W. Sher, Z. Lv, B. Luo, F. Jiang, T. Wu, C.-H. Ho, H.-C. Kuo, J.-H. He, Micro-light-emitting diodes with quantum dots in display technology. *Light: Sci. Appl.* **9**, 83 (2020).
31. Y. Cao, N. Wang, H. Tian, J. Guo, Y. Wei, H. Chen, Y. Miao, W. Zou, K. Pan, Y. He, H. Cao, Y. Ke, M. Xu, Y. Wang, M. Yang, K. Du, Z. Fu, D. Kong, D. Dai, Y. Jin, G. Li, H. Li, Q. Peng, J. Wang, W. Huang, Perovskite light-emitting diodes based on spontaneously formed submicrometre-scale structures. *Nature* **562**, 249–253 (2018).
32. Y. Bai, J. Qin, L. Shi, J. Zhang, M. Wang, Y. Zhan, H. Zou, S. Haacke, X. Hou, J. Zi, B. Hu, Amplified spontaneous emission realized by cogrowing large/small grains with self-passivating defects and aligning transition dipoles. *Adv. Opt. Mater.* **7**, 1900345 (2019).
33. L. Yang, L. Li, Q. Wang, C. Xing, L. Ma, Y. Zeng, Y. Zhao, Y. Yan, Over 1000-fold enhancement of the unidirectional photoluminescence from a microsphere-cavity-array-capped QD/PDMS composite film for flexible lighting and displays. *Adv. Opt. Mater.* **7**, 1901228 (2019).
34. A. G. Curto, G. Volpe, T. H. Taminiau, M. P. Kreuzer, R. Quidant, N. F. van Hulst, Unidirectional emission of a quantum dot coupled to a nanoantenna. *Science* **329**, 930–933 (2010).
35. D. V. Talapin, R. Koeppe, S. Gotzinger, A. Kornowski, J. M. Lupton, A. L. Rogach, O. Benson, J. Feldmann, H. Weller, Highly emissive colloidal CdSe/CdS heterostructures of mixed dimensionality. *Nano Lett.* **3**, 1677–1681 (2003).
36. A. Sitt, A. Salant, G. Menagen, U. Banin, Highly emissive nano rod-in-rod heterostructures with strong linear polarization. *Nano Lett.* **11**, 2054–2060 (2011).
37. X. Z. Qiao, X. Y. Chen, C. H. Huang, A. L. Li, X. Li, Z. L. Lu, T. Wang, Detection of exhaled volatile organic compounds improved by hollow nanocages of layered double hydroxide on Ag nanowires. *Angew. Chem. Int. Ed. Engl.* **58**, 16523–16527 (2019).
38. Z. Zhang, Y. Fu, W. Yu, X. Y. Qin, Z. J. Xue, Y. Liu, D. Luo, C. Yan, X. H. Sun, T. Wang, Dynamically regulated Ag nanowire arrays for detecting molecular information of substrate-induced stretched cell growth. *Adv. Mater.* **28**, 9589–9595 (2016).
39. C. Wang, Y. Wang, X. Su, V. G. Hadjiev, S. Dai, Z. Qin, H. A. C. Benavides, Y. Ni, Q. Li, J. Jian, M. K. Alam, H. Wang, F. C. R. Hernandez, Y. Yao, S. Chen, Q. Yu, G. Feng, Z. Wang, J. Bao, Extrinsic green photoluminescence from the edges of 2D cesium lead halides. *Adv. Mater.* **31**, 10 (2019).
40. J. H. Cha, J. H. Han, W. Yin, C. Park, Y. Park, T. K. Ahn, J. H. Cho, D. Y. Jung, Photoresponse of $CsPbBr_3$ and Cs_4PbBr_6 perovskite single crystals. *J. Phys. Chem. Lett.* **8**, 565–570 (2017).
41. D. M. Calistru, L. Mihut, S. Lefrant, I. Baltog, Identification of the symmetry of phonon modes in $CsPbCl_3$ in phase IV by Raman and resonance-Raman scattering. *J. Appl. Phys.* **82**, 5391–5395 (1997).
42. M. C. Brennan, M. Kuno, S. Rouvimov, Crystal structure of individual $CsPbBr_3$ perovskite nanocubes. *Inorg. Chem.* **58**, 1555–1560 (2019).
43. J. Liu, K. Song, Y. Shin, X. Liu, J. Chen, K. X. Yao, J. Pan, C. Yang, J. Yin, L.-J. Xu, H. Yang, A. M. El-Zohry, B. Xin, S. Mitra, M. N. Hedhili, I. S. Roqan, O. F. Mohammed, Y. Han, O. M. Bakr, Light-induced self-assembly of cubic $CsPbBr_3$ perovskite nanocrystals into nanowires. *Chem. Mater.* **31**, 6642–6649 (2019).
44. F. Bertolotti, G. Nedelcu, A. Vivani, A. Cervellino, N. Masciocchi, A. Guagliardi, M. V. Kovalenko, Crystal structure, morphology, and surface termination of cyan-emissive, six-monolayers-thick $CsPbBr_3$ nanoplatelets from X-ray total scattering. *ACS Nano* **13**, 14294–14307 (2019).
45. M. I. Bodnarchuk, S. C. Boehme, S. ten Brinck, C. Bernasconi, Y. Shynkarenko, F. Krieg, R. Widmer, B. Aeschlimann, D. Günther, M. V. Kovalenko, I. Infante, Rationalizing and controlling the surface structure and electronic passivation of cesium lead halide nanocrystals. *ACS Energy Lett.* **4**, 63–74 (2019).
46. Y. Chen, S. R. Smock, A. H. Flintgruber, F. A. Perras, R. L. Brutchey, A. J. Rossini, Surface termination of $CsPbBr_3$ perovskite quantum dots determined by solid-state NMR spectroscopy. *J. Am. Chem. Soc.* **142**, 6117–6127 (2020).
47. S. Toso, D. Baranov, C. Giannini, S. Marras, L. Manna, Wide-angle x-ray diffraction evidence of structural coherence in $CsPbBr_3$ nanocrystal superlattices. *ACS Mater. Lett.* **1**, 272–276 (2019).

Acknowledgments: TEM measurements were conducted at the Major Analytical Instrumentation Center at the Institute of Chemistry, Chinese Academy of Sciences. We thank X. Li (Institute of Chemistry, Chinese Academy of Sciences), J. Tai (Institute of Chemistry, Chinese Academy of Sciences), and L. Liang (Institute of Chemistry, Chinese Academy of

Sciences) for the data collection of TEM. X-ray scattering was conducted at the Beijing Synchrotron Radiation Facility. **Funding:** This work was supported by a National Science Foundation of China Grant (21925405), National Science Foundation of China Grant (201874005), and National Key Research and Development Program of China Grant (2018YFA0208800). **Author contributions:** Conceptualization: T.W. Methodology: T.W., X.L., and Z.X. Investigation: X.L., X.C., X.Q., G.M., W.B., and B.G. Funding acquisition: T.W. Discussion of data and useful suggestions: T.W., X.L., Z.X., G.M., W.B., and B.G. Supervision: T.W. Writing—original draft: T.W., X.L., and Z.X. Writing—review and editing: T.W., X.L., and B.G.

Competing interests: The authors declare that they have no competing interests. **Data and materials availability:** All data needed to evaluate the conclusions in the paper are present in the paper and/or the Supplementary Materials.

Submitted 25 May 2022
Accepted 26 September 2022
Published 11 November 2022
10.1126/sciadv.add1559